



HAL
open science

Exploring digital image correlation technique for the analysis of the tensile properties of all-cellulose composites

Feng Chen, Jean-Luc Bouvard, Daisuke Sawada, Christophe Pradille, Michael Hummel, Herbert Sixta, Tatiana Budtova

► **To cite this version:**

Feng Chen, Jean-Luc Bouvard, Daisuke Sawada, Christophe Pradille, Michael Hummel, et al.. Exploring digital image correlation technique for the analysis of the tensile properties of all-cellulose composites. *Cellulose*, 2021, 28, pp.4165-4178. 10.1007/s10570-021-03807-9 . hal-03188811

HAL Id: hal-03188811

<https://hal.science/hal-03188811v1>

Submitted on 20 Mar 2023

HAL is a multi-disciplinary open access archive for the deposit and dissemination of scientific research documents, whether they are published or not. The documents may come from teaching and research institutions in France or abroad, or from public or private research centers.

L'archive ouverte pluridisciplinaire **HAL**, est destinée au dépôt et à la diffusion de documents scientifiques de niveau recherche, publiés ou non, émanant des établissements d'enseignement et de recherche français ou étrangers, des laboratoires publics ou privés.

1

2 **Exploring Digital Image Correlation Technique for** 3 **the Analysis of the Tensile Properties of All-** 4 **Cellulose Composites**

5

6 Feng Chen ^a, Jean-Luc Bouvard ^b, Daisuke Sawada ^a, Christophe Pradille ^c, Michael
7 Hummel ^a, Herbert Sixta ^a, Tatiana Budtova ^{a, b*}

8

9 *^a Department of Bioproducts and Biosystems, School of Chemical Engineering,*
10 *Aalto University, P.O. Box 16300, 00076 Aalto, Helsinki, Finland;*

11 *^b MINES ParisTech, PSL Research University, Center for Materials Forming-*
12 *CEMEF, UMR CNRS 7635, CS 10207, 06904 Sophia Antipolis, France.*

13 *^c Mat Xper, 19 Traverse du Barri, 06560, Sophia Antipolis, France.*

14

15 * Correspondence: tatiana.budtova@mines-paristech.fr

16

17 **Abstract:** All-cellulose composites (ACCs) were prepared from filter paper via partial
18 dissolution in the ionic liquid 1-ethyl-3-methylimidazolium acetate, and material tensile
19 properties were investigated using various approaches. One is based on data directly taken
20 from a tensile testing machine, and the other uses two-cameras stereovision with digital
21 image correlation (DIC) technique. In the latter case, virtual extensometer with different
22 locations on the sample and averaging over sample surface were tested. Nominal and true
23 stress-strain dependences were built and Young's modulus, tensile strength, elongation at
24 maximal stress and toughness were evaluated as a function of ACC density. A minor
25 difference was observed for the stress-strain dependences derived from different
26 approaches which use the DIC technique, most probably because of low ACC deformation.
27 However, the results reveal that the nominal stress-strain curve from DIC is significantly
28 different from that which is directly derived from the data provided by machine sensors
29 thus strongly impacting Young's modulus and elongation at break values. This study
30 provides an insight into the evaluation of the mechanical properties of ACCs.

31 **Keywords:** *filter paper, ionic liquid, tensile properties, digital image correlation*

32

33 **1 Introduction**

34 The growing concerns on environmental issues motivate the development of
35 biobased and biodegradable materials such as biocomposites. One of the sub-
36 classes of biocomposites is all-cellulose composites (ACCs) (Nishino et al. 2004).
37 The principle of ACC fabrication is based on the concept of all-polymer composites
38 in which the matrix and the reinforcing fibers are made from the same matter
39 (Capiati and Porter 1975). The advantage of this concept is that the adhesion
40 between the matrix and the fibers is perfect, and there is no need of compatibilisers.
41 The difference between all-polymer and all-cellulose composites is that cellulose is
42 not melting, and thus ACC preparation requires a dissolution step followed by
43 washing out the solvent and drying.

44 There are two main routes for making all-cellulose composites: i) one-step
45 method via partial dissolution of fibers in cellulose solvent with the dissolved
46 cellulose forming the composite matrix (Soykeabkaew et al. 2008; Huber et al.
47 2012; Piltonen et al. 2016; Khakalo et al. 2019; Chen et al. 2020a) and ii) two-step
48 method which involves the preparation of a cellulose solution used for the
49 impregnation of the reinforcing fibers (Nishino et al. 2004; Spörl et al. 2017; Labidi
50 et al. 2019; Korhonen et al. 2019). In both cases the reinforcing phase can be natural
51 or man-made fibers, aligned or isotropic (dispersed short fibers, a fabric, or a filter
52 paper). Nanocellulose based composites will not be considered here as it is out of
53 the scope of this work.

54 Various cellulose solvents have been used to make ACCs:
55 LiCl/dimethylacetamide (DMAc) (Nishino et al. 2004; Soykeabkaew et al. 2008),
56 NaOH-water based solutions (Piltonen et al. 2016; Korhonen et al. 2019) and,
57 recently, ionic liquids (Spörl et al. 2017; Khakalo et al. 2019; Chen et al. 2020a).
58 For application reasons, the tensile properties of ACCs were always in the focus of
59 most of the publications. For example, when aligned native ramie fibers were
60 immersed in LiCl/DMAc for 2 h, exceptional longitudinal tensile properties of 460
61 MPa tensile strength and 28 GPa Young's modulus were obtained (Soykeabkaew
62 et al. 2008). One of the strongest man-made fibers, Bocell, was also used for making
63 ACCs with volume fractions of up to 90% of fibers, resulting in an average tensile
64 strength of 910 MPa and a Young's modulus of 23 GPa with 8% elongation at break
65 (Soykeabkaew et al. 2009). The above-mentioned mechanical properties far exceed

66 the values reported for the traditional unidirectional natural fiber reinforced
67 polymer composites. Nevertheless, the majority of the tensile properties of ACCs
68 lies in the interval of 1 – 20 GPa for Young’s modulus and 50 – 200 MPa for tensile
69 strength (Baghaei and Skrifvars 2020). The results depend on numerous parameters
70 such as the origin of the reinforcing fibers, their concentration and alignment, and
71 processing conditions (type of solvent, dissolution or impregnation time and
72 temperature, drying mode, etc.) (Baghaei and Skrifvars 2020). It should be noted
73 that the values obtained with tensile testing also depend on sample geometry and
74 the method used to obtain the specimen elongation (directly from the tensile
75 machine, from extensometer in which gauges are “clipped” on the material, using
76 video extensometers or digital image correlation (DIC)). We will not consider here
77 “contact” extensometer as it may induce damage or additional stress on the sample.
78 Mechanical analysis will be performed using DIC technique; for example, it is
79 commonly used for the analysis of the deformation mechanisms of polymers (Hild
80 and Roux 2006). This method is accurate and provides crucial information on the
81 strain field at macroscale level. It also allows measuring non-uniform deformation
82 and 3D effects. However, DIC is rarely used for natural fiber reinforced polymer
83 composites (Xu et al. 2019; Ramakrishnan et al. 2020) and, to the best of our
84 knowledge, was never considered for the evaluation of the tensile properties of all-
85 cellulose composites.

86 There are different ways to assess the tensile properties of a material. Below we
87 recall the background equations determining nominal stress (σ_n) and strain (ε_n):

$$88 \quad \sigma_n = \frac{F}{A_0} \quad (1)$$

$$89 \quad \varepsilon_n = \frac{d}{L_0} = \frac{L - L_0}{L_0} \quad (2)$$

90 where F is force, A_0 is cross-section area of the sample, d is displacement, and L_0
91 and L are the initial length of the sample and the length at a given applied force,
92 respectively. The displacement d can be monitored in different ways. One is using
93 data obtained from the machine displacement sensor; in this work such method will
94 be named “machine approach”. The other uses local measurement of sample
95 displacement, i.e. either with video extensometer or DIC techniques; it will be
96 named “local approach”.

97 Irrespective of the approach used, stress-strain dependences are built to
98 characterize the material with Young’s modulus in the linear region, maximal stress

99 (often called “tensile strength” or “ultimate stress”), elongation at break and
100 elongation at maximal stress. The as-obtained results will include different levels
101 of errors depending on the approach used. For instance, the measurement of
102 displacement made with the machine approach includes not only the elongation of
103 the sample in the gauge length region, but also the displacement induced by the
104 stiffness of the tensile machine, the last one inducing erroneous mechanical
105 properties (G’Sell et al. 1992). To exclude this problem which is common for all
106 tensile testing machines, non-contact measurements of the displacement were
107 developed. For example, video extensometer was introduced in the pioneering work
108 of G’Sell et al. (G’Sell et al. 1992) to study highly deforming materials showing
109 “necking”, the latter resulting in the alteration of the cross-section during
110 experiment. However, the displacement of the specimen may not be homogeneous
111 along the specimen length. The displacement measured using video extensometer
112 may depend on the location of the marks on the sample and also on the length L
113 which can be either sample length (eq.2) or the distance between selected two
114 points. Finally, the most precise (but the most time-consuming) way of having a
115 complete information on the deforming material is digital image correlation that
116 allows obtaining a map of local strains on the specimen surface due to video
117 cameras in stereovision which monitor the displacements of the markers (or
118 speckles) randomly placed on the sample surface (Sutton et al. 2009; Candau et al.
119 2016).

120 As far as all-cellulose composites are concerned, the majority of tensile
121 properties were obtained using a machine method (see, for example, ref.
122 Soykeabkaew et al. 2008; Soykeabkaew et al. 2009; Piltonen et al. 2016; Sirviö et
123 al. 2017; Korhonen et al. 2019; Wei et al. 2020; Chen et al. 2020a). Few works
124 report the results obtained with a video extensometer (Kröling et al. 2018; Mat
125 Salleh et al. 2017; Duchemin et al. 2009). In all examples mentioned above nominal
126 stress-strain dependences were used to calculate Young’s modulus, tensile strength
127 and elongation at break. The influence of the method on the stress-strain curves and
128 on the values of Young’s modulus, tensile strength and elongation at break of all-
129 cellulose composites has never been studied before.

130 The goal of this work was to analyse the tensile properties of all-cellulose
131 composites applying local and machine approaches and understand the influence of

132 each method on the values of the main mechanical characteristics of the material.
133 Filter paper-based ACCs were produced using the ionic liquid 1-ethyl-3-
134 methylimidazolium acetate ([EMIM][OAc]) as cellulose solvent, and the influence
135 of the dissolution time on composite morphology, density, crystallinity and optical
136 properties was investigated. Then, the tensile properties of ACCs were evaluated
137 using data obtained directly from the machine and with a local technique, the latter
138 using a two-cameras system and digital image correlation. Stress-strain data
139 corresponding to various approaches were obtained and discussed together with the
140 main tensile characteristics of the composite materials.

141 **2 Experimental Part**

142 **2.1 Materials**

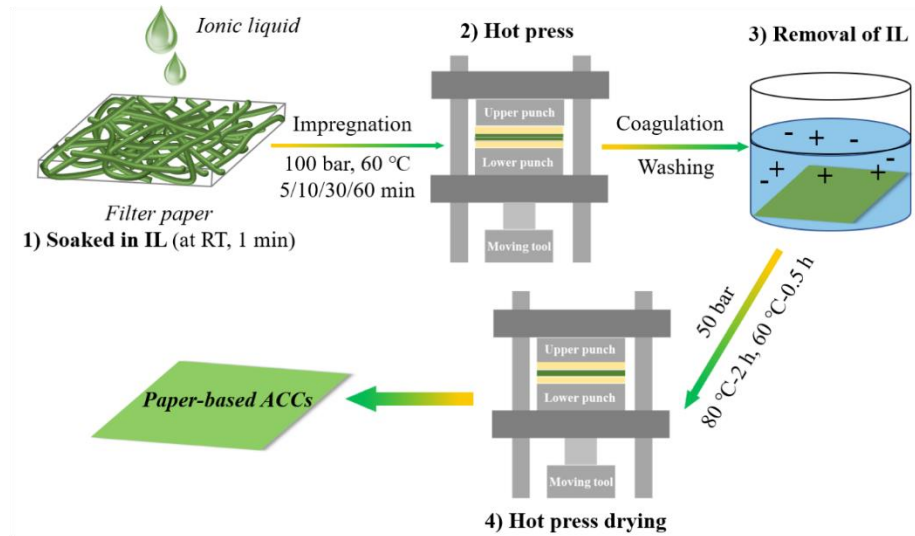
143 Qualitative VWR® Grade 415 filter paper made of pure cellulose was
144 purchased from VWR International, France. Ionic Liquid 1-ethyl-3-
145 methylimidazolium acetate ([EMIM][OAc], purity > 95%) was purchased from
146 IoLiTec. The initial moisture content is 0.27 wt.%, determined by Karl-Fischer
147 titration. The IL was used as received. Water used in this study was deionized.

148 **2.2 Methods**

149 *2.2.1 Manufacturing paper-based ACCs*

150 The paper-based ACCs manufacturing method is illustrated in Figure 1. Two
151 pieces of filter papers were dipped in [EMIM][OAc] for 1 min, stacked together
152 and hot pressed at 60 °C. The pressing times were 5 min, 10 min, 30 min and 60
153 min with the pressure kept constant (around 100 bar). Then the sample was
154 immersed in a large amount of deionized water for about 72 h (exchanging to fresh
155 water every day) to remove the ionic liquid from the system. Finally, the specimen
156 was dried by hot pressing (around 50 bar, 80 °C for 2.5 h and then at 60 °C for 0.5
157 h). A temperature gradient during drying was shown to prevent the warping and/or
158 heterogeneous contraction of the sample (Chen et al. 2020a). ACCs produced with
159 5 min, 10 min, 30 min and 60 min impregnation are named P5, P10, P30 and P60,
160 respectively.

161



162

163

Fig. 1 Illustration of the fabrication of the paper-based ACCs

164

165 2.2.2 Scanning electron microscopy (SEM)

166 The surface and cross-section morphologies of the filter paper and produced
 167 ACCs were observed using a scanning electron microscope (Zeiss Sigma VP FE-
 168 SEM) at an accelerating voltage of 4 kV. Prior to examination, the surface and cross
 169 section of the samples were coated with a thin layer of gold.

170 2.2.3 Sample thickness and density

171 The density of the filter paper and of the produced ACCs was determined by
 172 measuring sample weight and volume. The volume was calculated from the
 173 dimensions of the sample measured by using L&W Micrometer (Lorentzen &
 174 Wettre Products, ABB, Switzerland) with an error of $\pm 1 \mu\text{m}$ or 0.1 % of reading
 175 whichever is greater. Porosity was estimated from the density of filter paper and
 176 ACCs by using a value of 1.47 g cm^{-3} as the density of cellulose (Sun 2008), using
 177 the following equation:

$$178 \quad \text{Porosity (\%)} = \left[1 - \frac{\rho_{\text{ACCs}}}{\rho_{\text{cellulose}}} \right] \times 100\% \quad (3)$$

179 2.2.4 Ultraviolet–Visible Light (UV–vis) Spectroscopy

180 The transmittance and haze of the nanopapers in the visible light region were
181 obtained using a Shimadzu UV-2600 with an ISR-2600 Plus Integrating Sphere
182 Attachment (Shimadzu, Japan). Optical haze was used to quantify the percentage
183 of the forward light scattering as follows:

$$184 \quad \text{Haze} = \left[\frac{T_4}{T_2} - \frac{T_3}{T_1} \right] \times 100\% \quad (4)$$

185 where T_1 , T_2 , T_3 and T_4 are defined as background checking, total transmitted
186 illumination, beam checking and pure diffusive transmittance, respectively.

187 2.2.5 X-ray diffraction (XRD)

188 XRD data were collected in the reflection mode of an X-ray instrument,
189 SmartLab (RIGAKU), operated at 45 kV and 200 mA. The sample was placed on
190 a sample holder horizontally to incident X-ray and the scans were performed in the
191 2θ range from 5° to 60° by $\theta/2\theta$ mode. Background intensity profile without sample
192 was collected in the same conditions, and it was subtracted from the obtained data.
193 The subtracted data were corrected for the Lorentz-polarization factor for each data
194 point. The background intensity (S_{bkg}) from the amorphous phase of cellulose was
195 estimated by robust smoothing procedure as described elsewhere. The total
196 crystallinity index (CRI) of the initial filter paper and of ACCs was estimated using
197 the ratio of the area of total intensity (S_{total}) to that of background intensity S_{bkg} in
198 the 2θ range from 10° to 32° :

$$199 \quad \text{CRI, \%} = 100\% \times \left(1 - \frac{S_{\text{bkg}}}{S_{\text{total}}} \right) \quad (5)$$

200 The background-corrected profile was fitted with 4 pseudo-Voigt function for
201 cellulose I ((1-10), (110), (102)/(012) and (200) lattice planes) and 3 pseudo-Voigt
202 functions for cellulose II ((1-10),(110) and (020) lattice planes). For each
203 polymorph, the ratio of amplitude for the lattice planes were fixed to be the ratio of
204 the square of structure factor (Nishiyama et al. 2002, Langan et al. 2001). The
205 deviation of diffraction positions was limited to be close to those calculated from
206 the unit cell parameters of the crystal structure of cellulose I and II. The software
207 LMFIT (Newville et al. 2016) was used for the fitting. As the mass absorption
208 coefficients are identical for crystalline polymorphs, quantitative phase analysis
209 was performed using the single peaks of cellulose polymorphs (Alexander and Klug

210 1984). The intensities for the 1–10 lattice plane of cellulose I ($I_{1-10(1)}$) and cellulose
 211 II ($I_{1-10(2)}$) can be expressed as a function of the structure factor $F_{1-10(\alpha)}$, the volume
 212 of unit cell $V_{(\alpha)}$ and the volume fraction v_{α} of each crystalline phase (α being either
 213 cellulose I or II crystal) in the total cellulose crystal, as follows:

$$I_{1-10(\alpha)} = \frac{K}{V_{(\alpha)}^2} |F_{1-10(\alpha)}|^2 v_{\alpha} \quad (6)$$

214 where K is a constant for the instrument and sample.

215 Thus, the ratio of the volume fraction of cellulose II to cellulose I, v_2/v_1 , is as
 216 follows:

$$\frac{v_2}{v_1} = \frac{2.27 I_{1-10(2)}}{I_{1-10(1)}} \quad (7)$$

217 where the coefficient 2.27 was calculated from the unit cell volume and the structure
 218 factor for the 1–10 lattice of cellulose I (Nishiyama et al. 2002) and cellulose II
 219 (Langan et al. 2001). This equation was used to calculate the volume fraction of
 220 cellulose II over the total crystalline cellulose as follows:

$$Cell_{II} \text{ vol } \% = \frac{v_2}{v_1 + v_2} \quad (8)$$

221 2.2.6 Tensile Testing

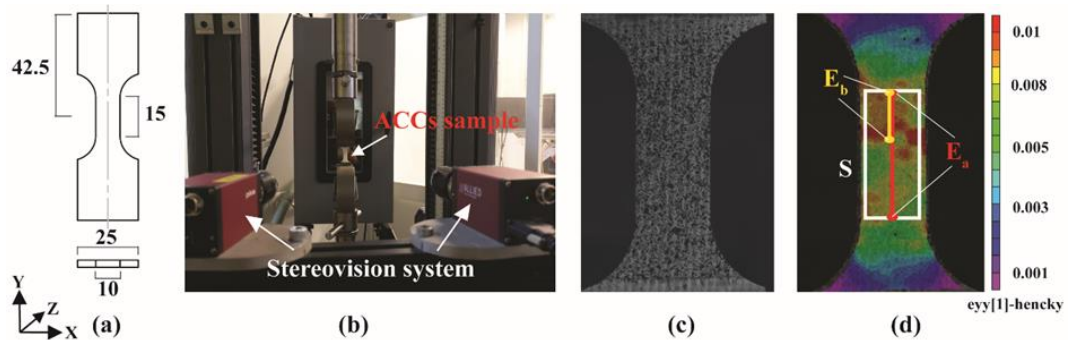
222 The mechanical properties of the filter paper and ACCs were studied using the
 223 electro-mechanical tensile test machine Zwick-2.5kN at 23 °C and 50% relative
 224 humidity. Figure 2a presents the geometry of the tensile sample with a gauge length
 225 (L_0) and a width (W) of 15 mm and 10 mm, respectively. Sample thickness was
 226 measured at different locations within the gauge length area for each sample with
 227 high-precision caliper and the maximal standard deviation was ± 0.005 mm/50 mm.
 228 The tensile measurements were carried out at a strain rate of $1 \times 10^{-3} \text{ s}^{-1}$.

229 The first set of force-displacement data was collected directly from the tensile
 230 machine (machine approach). In parallel, two-cameras stereovision system was
 231 used to monitor the local displacements of ACC (Figure 2b). Stereovision provides
 232 a 3D image of sample surface using a superposition of two 2D plane images, and
 233 DIC allows building a 2D displacement field on sample surface. In this work, a 3D
 234 DIC method was used. The advantages of 3D DIC method compared to the 2D DIC
 235 can be found elsewhere (Sutton et al. 2008). The calibration of 3D DIC was done
 236 until a projection error of 0.05 was reached (Sutton et al. 2009).

237 To monitor the local displacements, the front surface of the sample was coated
 238 with a thin layer of white paint on which black ink was sprayed to generate a random
 239 speckle pattern (Figure 2c). The displacement field was obtained by tracking the
 240 positions of speckle patterns on a specimen surface before and after the deformation
 241 of the body. Practically, two sets of images – corresponding to two different
 242 mechanical states (i.e. reference and deformed) – are recorded by two fixed cameras
 243 set with in-between fixed angle. As grey level cannot be a unique characteristic of
 244 a “point” on sample surface, neighboring pixels must be used to build a
 245 displacement field using the initial and deformed pictures. Such a collection of pixel
 246 values is called a subset. Large speckles (e.g. more than 20 pixels) were avoided as
 247 they need large subset sizes which reduces the spatial resolution of the analysed
 248 zone.

249 The displacement fields were built from images recorded by a pair of cameras
 250 AVT PIKE 5 Megapixels with a 2/3' CCD sensors and 50 mm Schneider
 251 Kreuzwach objectives. The images were taken every second and post-processed
 252 using VIC-3D software (S. Vic-3D 2007) (Figure 2d). The first step of the analysis
 253 consists of creating a regular mesh in the region of interest. The meshing allows
 254 tracking the speckle pattern during the tensile test. In this study, the subset was 23
 255 pixels with a step of 5 and filter size of 13. More details on the selection of
 256 parameters and analysis of data are given in the Supporting Information.

257



258

259 **Fig. 2** The tensile testing setup used in this study: (a) geometry of a tensile sample,
 260 values are in mm; (b) experimental setup with stereovision system; (c) speckled
 261 sample for the DIC analysis and (d) example of true strain field obtained by DIC
 262 analysis using VIC-3D software, E_a and E_b are locations of a virtual extensometer

263 and S is the surface of the rectangle over which the true strain in the longitudinal
264 direction is averaged

265 As mentioned in the Introduction, there are different ways of using digital image
266 correlation approach. One option is to use it as a video extensometer: we select two
267 different locations of “virtual extensometers”, one monitoring strain evolution
268 along E_a and the other along E_b (Figure 2d). Different locations of the virtual
269 extensometers are selected to better understand the influence of their location on
270 strain distribution over the sample and the corresponding stress-strain dependences.
271 Another option is to average the displacement over a given surface; here we will
272 use surface S shown by a rectangle in Figure 2d. While virtual extensometer
273 provides nominal strain evolution over time and further nominal stress-strain
274 response (eq. 1 and 2), the evolution of true strain over time is obtained from VIC-
275 3D software by averaging true strain distribution over the surface S. We recall
276 below the relationship between true strain ε_{true} and nominal strain ε_n :

$$277 \quad \varepsilon_{true} = \ln\left(1 + \frac{L - L_0}{L_0}\right) = \ln(1 + \varepsilon_n) \quad (9)$$

278 true stress σ_{true} is then determined as follows:

$$279 \quad \sigma_{true} = \frac{F}{A(t)} = \frac{F}{A_0 \exp(-\varepsilon_{true})} \quad (10)$$

280 where $A(t)$ is sample cross-section area at a given moment.

281

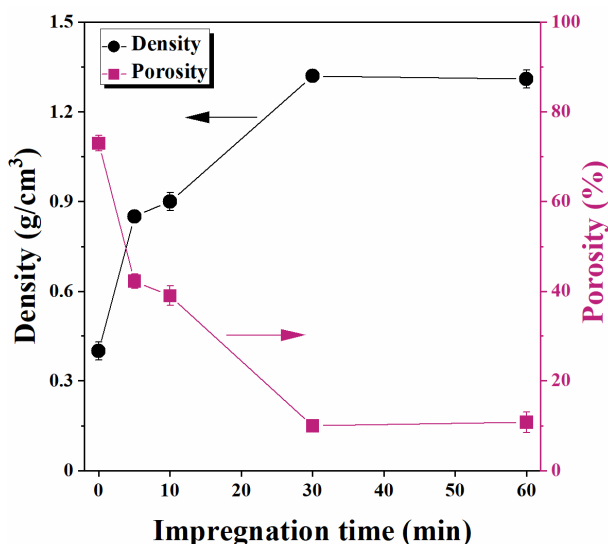
282 **3 Results and Discussions**

283 To better understand the mechanical performance of ACCs and the influence of
284 the analysis method (machine vs local), material properties such as density,
285 morphology and crystallinity must be first examined. Therefore, we start with the
286 analysis of the evolution of ACC characteristics as a function of processing
287 conditions. Then, the local approach using different DIC analyses vs machine
288 approach applied to ACC will be addressed, using one sample as an example. This
289 study will be used to setup the methodology of tensile tests analysis. Finally, the
290 tensile values (tensile (maximal) strength, strain at maximal strength, Young’s
291 modulus and work of fracture) obtained via machine data and local approach using
292 stereovision system are compared and discussed.

293

294 3.1 Density and crystallinity of ACCs

295 The evolution of ACC density and porosity as a function of impregnation time
296 is shown in Figure 3. Density increases with the impregnation time under pressure
297 indicating a strong decrease in material porosity, from 73% for filter paper and 42%
298 for P5 to 11% for P60 (Figure 3). No noticeable evolution is recorded after 30 min
299 of dissolution.

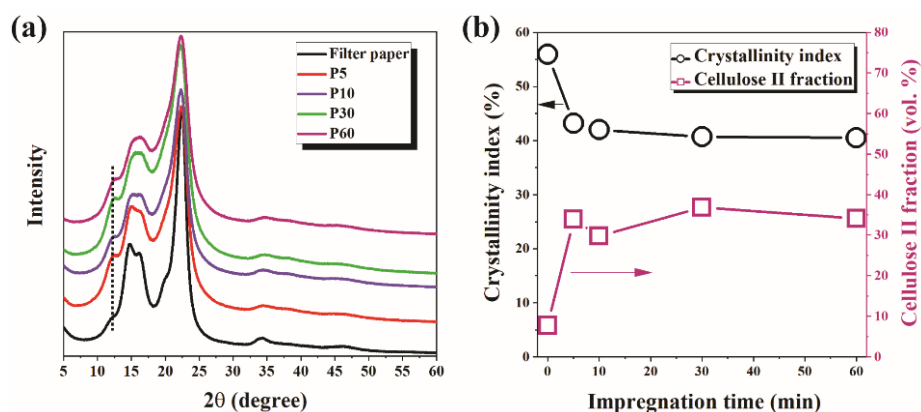


300

301 **Fig. 3** Density and porosity of ACC as a function of impregnation time. The
302 properties of filter paper are shown at $t = 0$. The lines are given to guide the eye

303 The ACCs XRD profiles, crystallinity and cellulose allomorphs as a function of
304 impregnation time are shown in Figure 4. The filter paper was theoretically
305 composed of native cellulose which is the cellulose I allomorph. However, a small
306 diffraction peak at $2\theta \approx 12^\circ$, which indicates cellulose II allomorph, was also
307 observed (Figure 4a). It has been reported that a paper sheet, despite supposed to
308 be native cellulose, may contain a small amount of cellulose II crystalline structure
309 (Sirviö et al. 2017; Piltonen et al. 2016). The amount of cellulose II strongly
310 increases after 5 min impregnation, from around 7 to 34 vol%, but then does not
311 vary significantly (Figure 4b). Crystallinity drops from around 56% to 43% for 5
312 min impregnation and then slowly decreased to around 40% for longer
313 impregnation times. Based on these results we suppose that dissolution was almost
314 stopped after the first 5 minutes. The reason is that the total cellulose concentration
315 was too high (> 40 wt.%), above the dissolution limit in the ionic liquid. It was
316 suggested that at least 3 ionic liquid molecules per anhydroglucose unit are needed

317 to dissolve cellulose in [EMIM][OAc] which corresponds to a maximum cellulose
318 solubility of around 25-27 wt.% (Le et al. 2014). It should also be taken into account
319 that the viscosity of the dissolved phase is high and dissolution (impregnation) was
320 performed in static conditions, without mixing, also preventing cellulose
321 dissolution.
322



323

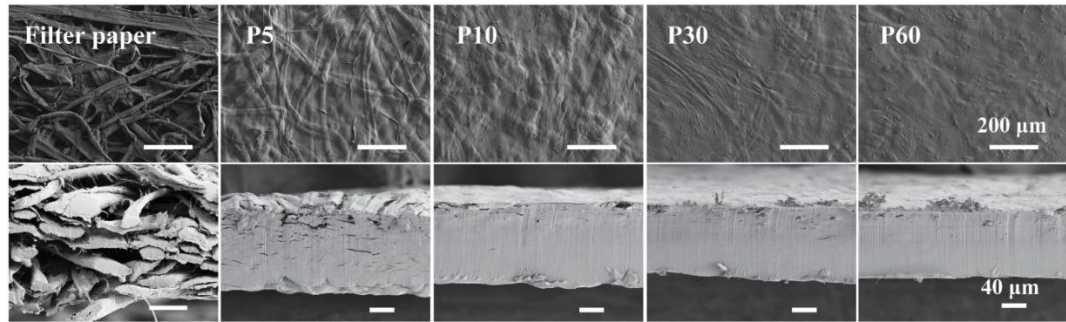
324 **Fig. 4** (a) X-ray diffractograms of filter paper and the produced ACCs, the black
325 dotted line indicates the characteristic peak of cellulose II. (b) The total crystallinity
326 index and cellulose II volume fraction of ACC as a function of impregnation time,
327 the lines are given to guide the eye. The properties of filter paper are shown at $t =$
328 0

329 3.2. Morphology and optical properties of the ACCs

330 To provide a direct evidence of the gradient dissolution of the fibers in the filter
331 paper induced by the impregnation time and compression, the surface and cross-
332 section morphologies of the initial paper and of obtained ACCs were examined by
333 SEM (Figure 5). The starting material shows individual fibers typical for a filter
334 paper with large number of voids, as confirmed by the low density. After 5 min of
335 impregnation, fibers can still be distinguished (Figure 5, images of the surface on
336 the top row) but they are well embedded into the dissolved cellulose matrix
337 demonstrating excellent adhesion. The cross-section shows some remaining pores
338 (Figure 5, lower row). After 10 min and longer impregnation times the fibrous
339 structure of the paper had almost disappeared and no pores can be seen. Figure 5
340 also shows the decrease of ACCs cross-section. SEM observations are in-line with
341 density and XRD results: cellulose that could be dissolved was dissolved during the

342 first 5 minutes (strong increase of cellulose II fraction and drop of crystallinity) and
343 further morphology evolution is due to the distribution of dissolved phase within
344 the pores under pressure (no evolution of cellulose II fraction and crystallinity but
345 continuous increase in density).

346

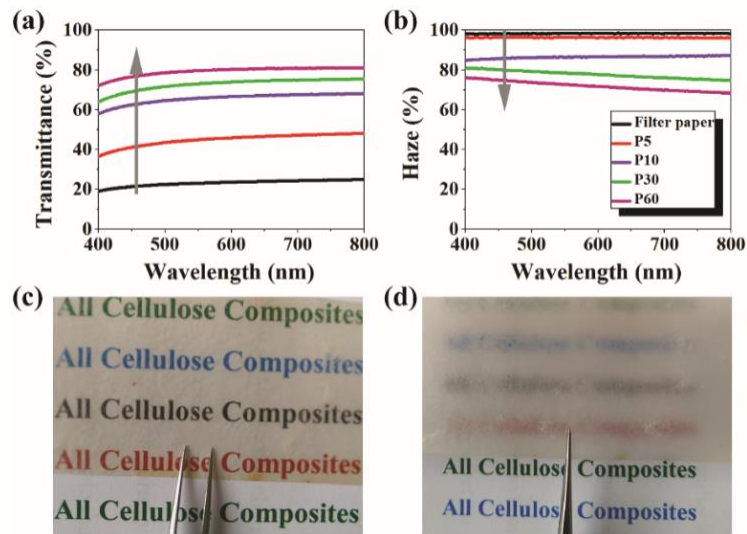


347

348 **Fig. 5** (a) Upper set of images: the surface of filter paper and ACCs P5, P10, P30
349 and P60; (b) lower set of images: cross-section of filter paper and of the
350 corresponding ACCs. The scale bar for all images on the upper set is 200 μm and
351 on the lower set 40 μm

352 The optical properties of ACCs are correlated with their morphology. Figure 6
353 displays the optical transmittance and haze of the filter paper and the as-prepared
354 ACCs. As the filter paper consists of randomly packed irregular cellulose fibers and
355 micron-size voids, it is opaque in the visible light due to massive backward light
356 scattering and possess almost 100% transmission haze because of strong forward
357 light scattering. In ACCs, the dissolved cellulose fills the voids with the matter of
358 the same refractive index as fibers, surface roughness is decreased and the material
359 becomes transparent in the visible light (Figure 6a). Morphology homogenization
360 also decreases the forward light scattering resulting in the reduction of haze (Figure
361 6b). Both transmittance and haze show a sharp transition of properties at
362 impregnation times longer than 5 min, in-line with the ACC morphology (Figure 5)
363 and density (Figure 4). It is worth noting that ACCs P60 is transparent (optical
364 transmittance $\sim 80\%$ at 550 nm) but still with high haze ($> 70\%$ at 550 nm), which
365 makes it promising as photonic material for optoelectronic applications such as
366 solar cells, as haze increases light scattering and absorption (Hou et al. 2020; Chen
367 et al. 2020b). The digital photographs of ACC P60 confirm high transmittance and
368 high haze (Figure 6c, d).

369



370

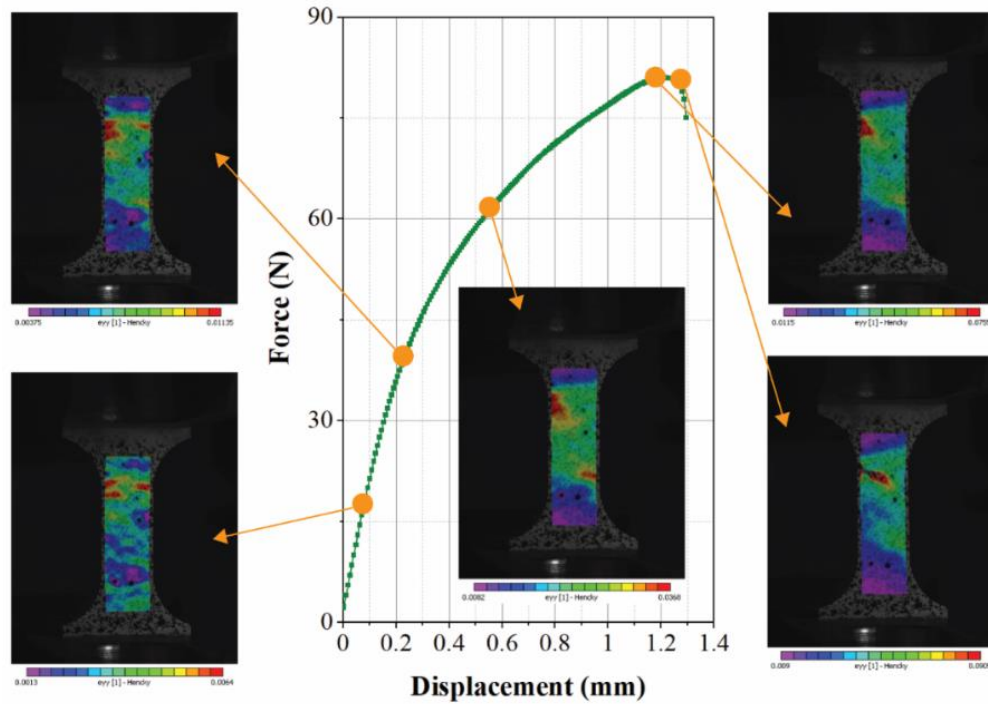
371 **Fig. 6** Optical transmittance (a) and haze (b) of filter paper and the ACCs, ACC
372 P60 in close contact with the colored letters underneath to show its high light
373 transmittance (c) and 1 cm away from the same substrate (d) to indicate its high
374 haze

375

376 3.3 Mechanical properties

377 3.3.1 Local vs machine approach

378 Sample P5 was used to test different approaches for the analysis of ACC tensile
379 properties. An example of strain distributions over the sample surface obtained with
380 a local (DIC) approach for tensile loading is shown in Figure 7. This type of analysis
381 was performed for all other samples. Figure 7 shows that the strain field is
382 heterogeneous with strain concentration on the upper side; failure is initiated in this
383 area.



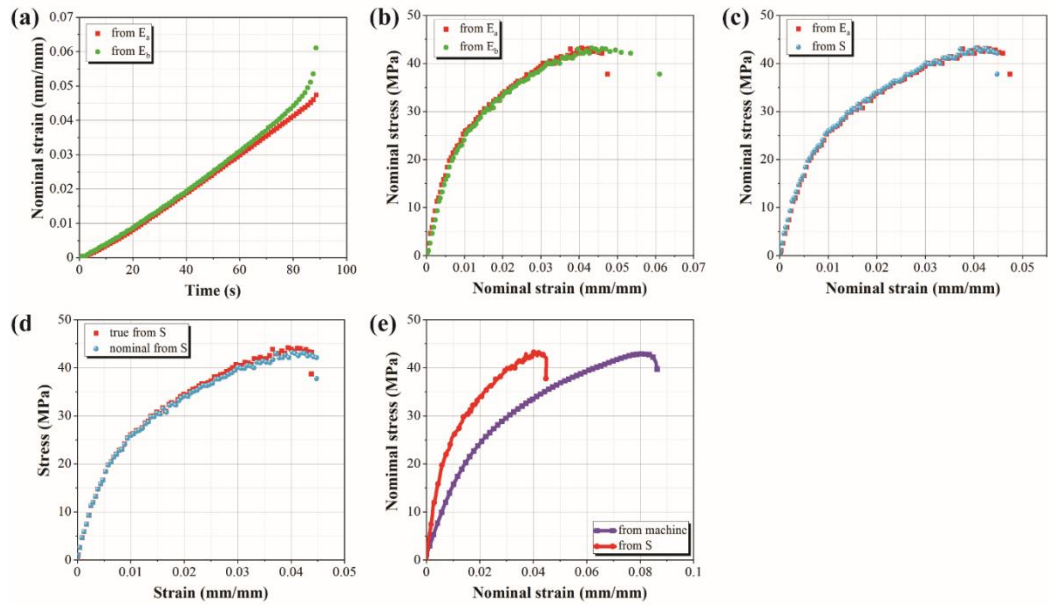
384

385 **Fig. 7** The true strain field in the longitudinal direction obtained by DIC as function
 386 of displacement for the sample P5

387

388 To check if this heterogeneity induces differences in stress-strain curves, the
 389 nominal strain was plotted as a function of time (Figure 8a) and then converted into
 390 nominal stress-strain curves (Figure 8b) for two locations of the virtual
 391 extensometer, E_a and E_b (see details Methods section). Figure 8a shows similar
 392 curves for the two positions until a strain of 0.03. Some differences are then
 393 observed due to the strong localisation of the deformation and the specimen failure.
 394 It is translated into a quite minor difference in the strain at failure, 0.06 (for E_b) vs
 395 0.05 (for E_a). The strain localisation is well captured by E_b while E_a , characterized
 396 by a higher gauge length L_0 , is less sensitive to this strain localisation and as it
 397 represents the average of the nominal strain distribution over the corresponding
 398 gauge length. As stress-strain curves are practically identical, Young's modulus and
 399 tensile strength are the same for both locations of the virtual extensometer. However,
 400 this may not always be the case especially for the determination of the strain to
 401 failure.

402



403

404 **Fig. 8** Comparisons of tensile data for P5 obtained with different approaches: (a)
 405 nominal strain as a function of extension time collected from the virtual
 406 extensometers E_a and E_b , (b) nominal stress-strain curves from the virtual
 407 extensometers E_a and E_b ; (c) nominal stress-strain curves from the virtual
 408 extensometer E_0 and over the surface S ; (d) nominal and true stress-strain curves
 409 obtained with stereovision system over the surface S and (e) nominal stress-strain
 410 curves obtained from the machine and with stereovision system over the surface S

411

412 Next, we compare nominal stress-strain curve obtained from the virtual
 413 extensometer E_a with that averaged over the surface S (Figure 8c). A minor
 414 difference is observed for the strain at failure. Then nominal and true stress-strain
 415 curves are compared for the case when the strain averaged over the surface S
 416 (Figure 8d). The true stress is slightly higher than the nominal one with slightly
 417 lower strain at failure. Such coincidence can be explained by the overall low
 418 deformation of the sample. For materials exhibiting large deformations more
 419 differences between nominal and true strain-stress curves are usually recorded.

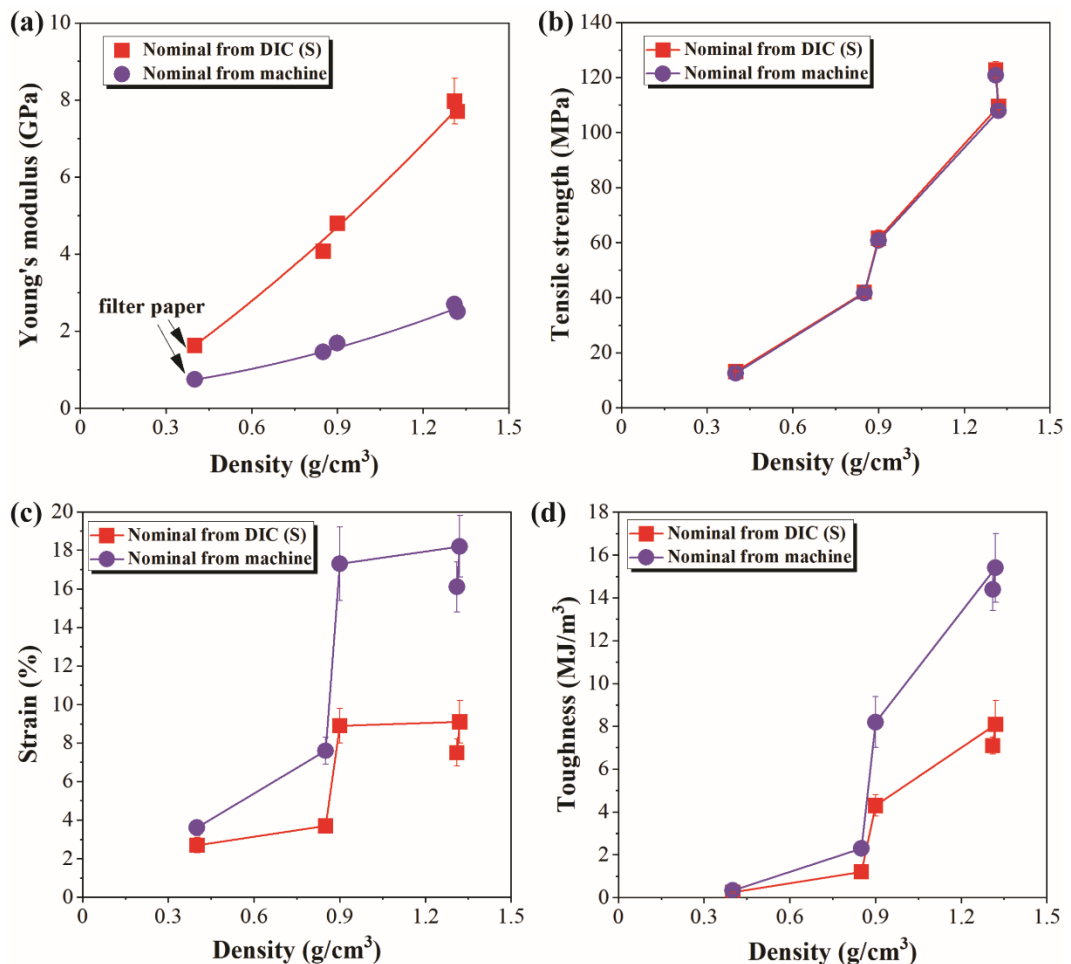
420 Finally, Figure 8e compares the nominal stress-strain curve directly derived
 421 from the machine (machine approach) with that derived from stereovision and
 422 averaged over the surface S (local approach). Here the difference is significant: the
 423 strain at failure determined with machine approach is twice higher than that
 424 determined with DIC. With nominal tensile strength being almost the same,

425 Young's modulus calculated with the local approach will be much higher than that
426 calculated from machine approach. We remind that the latter provides results with
427 the systematic error arising from the equipment input.

428 3.3.2 Tensile properties of ACCs

429 Young's modulus, tensile strength, strain at maximal stress and toughness were
430 calculated from nominal and true stress-strain curves (Figure S1, Supporting
431 Information) derived from the machine and local approaches, the latter using
432 stereovision system and averaged over the surface S. All mechanical characteristics
433 of the filter paper and ACCs are given in Table S1, their dependence on material
434 density is shown in Figure 9 and on the impregnation time in Figure S2.

435



436

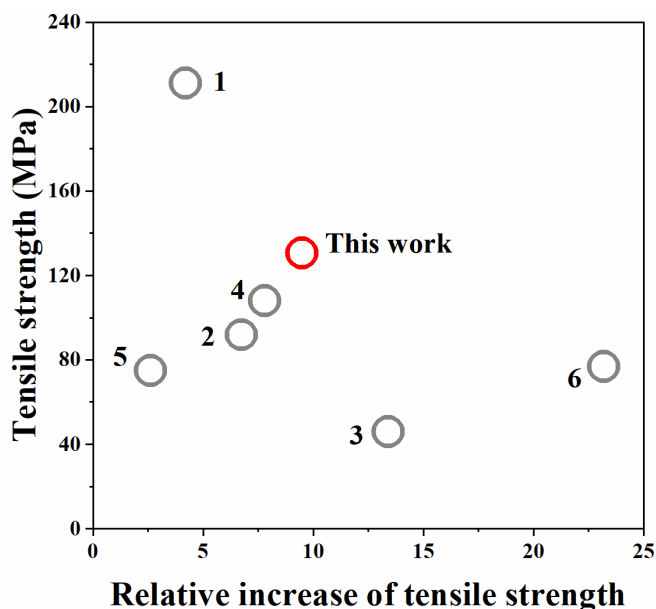
437 **Fig. 9** Young's modulus, tensile strength, strain at maximal stress and toughness of
438 the filter paper and ACCs as a function of density. When errors are not visible, they
439 are within the size of the symbol. The lines are given to guide the eye

440 The increase in ACC density, which corresponds to the increase of
441 impregnation time, leads to a strong increase of Young's modulus, independent of
442 the method used to determine it (Figure 9a). All values calculated from nominal
443 stress-strain curves via a local approach using stereovision are much higher than
444 those calculated from nominal ones via machine approach, as expected from Figure
445 8e. We also plotted Young's modulus as a function of crystallinity (Figure S3);
446 modulus decrease with crystallinity increase shows that the crystallinity does not
447 play an important role here as it is the presence of pores and heterogeneities that
448 control mechanical properties. It has been demonstrated in the previous studies that
449 density plays the essential role in the mechanical performance of ACCs (Korhonen
450 et al. 2019; Chen et al. 2020a); an adequate comparison with literature can thus be
451 made only for the materials either of the same density or for the specific values of
452 mechanical characteristics. Unfortunately, the density of ACC is not always
453 reported. To the best of our knowledge, for paper-based isotropic all-cellulose
454 composites, only the study from Piltonen et al. (Piltonen et al. 2016) reported
455 density values. The calculated specific strength and modulus values obtained in this
456 work are listed in Table S2 in the Supporting Information and compared with those
457 reported by Piltonen et al. (Piltonen et al. 2016). Considering that the type of
458 approach (machine or contact or non-contact extensometer) is rarely specified, the
459 comparison of moduli values with the results obtained in literature becomes even
460 more delicate.

461 Similar to the Young's modulus, tensile strength and toughness increase with
462 density increase. Interestingly, the strain at break also increases, from 4 to 9%, the
463 latter corresponding to the ACC with a density of around 0.9 g/cm^3 (impregnation
464 time 10 min); at higher density, the strain at break remains on the same level. A
465 certain porosity improves material ductility.

466 Figure 8 and 9 show that while Young's modulus calculated from nominal
467 stress-strain curves using a local approach is higher than that calculated using the
468 machine approach, the opposite was obtained for the strain at maximum stress and
469 toughness. A lower toughness obtained from local approach is due to much lower
470 nominal strains at maximum stress as compared to those obtained via machine
471 approach. Tensile strength values did not depend on the approach used within the
472 errors.

473 Overall, a simple strategy of filter paper impregnation with ionic liquid for 30-
474 60 min allowed increasing the tensile strength by almost 10 times, of Young's
475 modulus by 5 times and of toughness by 25 times as compared to the initial filter
476 paper. In order to make an adequate comparison with literature results, the
477 properties of the starting material should be considered. In our case, the nominal
478 tensile strength values calculated from the local approach and from machine
479 approach are similar. Supposing this is the case for ACCs published in other works,
480 the results on various isotropic ACCs can be put together. As presented in Figure
481 10, Sirviö et al. (Sirviö et al. 2017) obtained a very high increase of nominal tensile
482 strength of dissolving pulp-based ACCs, up to 24 times, but the absolute value of
483 tensile strength was only around 76 MPa, most probably because of the low
484 mechanical properties of the starting material. Nishino and Arimoto (Nishino and
485 Arimoto 2007) reported a filter paper-based ACC with a nominal highest tensile
486 strength of 211 MPa, but the initial filter paper was much stronger, with tensile
487 strength around 50 MPa. In the current study the tensile strength of the initial filter
488 paper was around 13 MPa. The comparison of the best values of tensile strength vs
489 its increase as compared to the strength of the initial paper is shown in Figure 10.
490



491

492 **Fig. 10** A comparison of maximal tensile stress and of the increase of maximal
493 tensile stress as compared to the starting filter paper for isotropic paper-based ACCs

494 (1, Nishino and Arimoto 2007; 2, Duchemin et al. 2009; 3, Piltonen et al. 2016; 4,
495 Wei et al. 2020; 5, Han and Yan 2010; 6, Sirviö et al. 2017)

496

497 **4 Conclusions**

498 All-cellulose composites were made via controlled impregnation with ionic
499 liquid, [EMIM][OAc]. First, the properties of the composites (density, porosity,
500 crystallinity, cellulose II fraction, transmittance, haze and morphology) were
501 investigated as a function of impregnation time. The results showed that cellulose
502 was dissolved during the first 5 minutes, and further evolution of properties was
503 due to the distribution of dissolved phase within the pores.

504 Tensile testing was conducted using different methods to obtain the specimen
505 elongation: i) data directly taken from machine sensors and ii) using digital image
506 correlation technique and local approach. The latter excludes the errors related to
507 the stiffness of the tensile testing machine itself. Although the nominal tensile
508 strength values from DIC and machine are similar, the nominal Young's modulus,
509 strain at maximal stress and, as a consequence, toughness, are very different. This
510 must be taken into account when comparing results from different literature sources.
511 ACC fabrication strategy using in this work resulted in the increase of tensile
512 strength, Young's modulus and toughness by almost 10, 5 and 25 times,
513 respectively, as compared to the initial filter paper.

514

515 **Acknowledgements:** The financial support from Business Finland (Grant No.
516 211599), FinnCERES funding, Foundation for Aalto University Science and
517 Technology, Stora Enso Oyj and UPM-Kymmene Oyj is gratefully acknowledged.
518 Authors wish to thank Separation Research Oy Ab and Fibertus Oy for
519 collaboration. We also acknowledge the provision of facilities and technical support
520 by Aalto University at OtaNano-Nanoscience Center (Aalto-NMC).

521

522 **Declarations**

523

524 **Funding:** Business Finland (Grant No. 211599), FinnCERES funding, Foundation
525 for Aalto University Science and Technology, Stora Enso Oyj and UPM-Kymmene
526 Oyj

527

528 **Conflicts of interest:** not applicable

529 **Availability of data and material:** data can be provided upon request

530 **Code availability:** not applicable

531

532 **References**

- 533 Alexander L, Klug HP (1948) Basic aspects of X-ray absorption in quantitative diffraction analysis
534 of powder mixtures. *Anal Chem* 20:886–889.
- 535 Baghaei B, Skrifvars M (2020) All-Cellulose Composites: A Review of Recent Studies on Structure,
536 Properties and Applications. *Molecules* 25:2836.
- 537 Candau N, Pradille C, Bouvard JL, Billon N (2016) On the use of a four-camera stereovision system
538 to characterize large 3D deformation in elastomers. *Polym Test* 56:314-20.
- 539 Capiati NJ, Porter RS (1975) The concept of one polymer composites modelled with high density
540 polyethylene. *J Mater Sci* 10:1671–1677.
- 541 Chen F, Sawada D, Hummel M, Sixta H, Budtova T (2020a) Unidirectional All-Cellulose
542 Composites from Flax via Controlled Impregnation with Ionic Liquid. *Polymers* 12:1010.
- 543 Chen F, Xiang W, Sawada D, Bai L, Hummel M, Sixta H, Budtova T (2020b) Exploring Large
544 Ductility in Cellulose Nanopaper Combining High Toughness and Strength. *ACS Nano*
545 14:11150–11159.
- 546 Duchemin BJ, Mathew AP, Oksman K (2009) All-cellulose composites by partial dissolution in the
547 ionic liquid 1-butyl-3-methylimidazolium chloride. *Compos Part A-Appl S* 40:2031-7.
- 548 G'Sell C, Hiver JM, Dahoun A, Souahi A (1992) Video-controlled tensile testing of polymers and
549 metals beyond the necking point. *J Mater Sci* 27:5031-9.
- 550 Han D, Yan L (2010) Preparation of all-cellulose composite by selective dissolving of cellulose
551 surface in PEG/NaOH aqueous solution. *Carbohydr Polym* 79:614-9.
- 552 Hild F, Roux S. Digital image correlation: from displacement measurement to identification of
553 elastic properties-a review. *Strain*. 2006 May;42(2):69-80.
- 554 Hou G, Liu Y, Zhang D, Li G, Xie H, Fang Z (2020) Approaching Theoretical Haze of Highly
555 Transparent All-Cellulose Composite Film. *ACS Appl Mater Interfaces* 12:31998-2005.
- 556 Huber T, Bickerton S, Mussig J, Pang S, Staiger MP (2012) Solvent infusion processing of all-
557 cellulose composite materials. *Carbohydr Polym* 90:730–733.
- 558 Khakalo A, Tanaka A, Korpela A, Hauru LKJ, Orelma H (2019) All-Wood Composite Material by
559 Partial Fiber Surface Dissolution with an Ionic Liquid. *ACS Sustain Chem Eng* 7:3195–
560 3202.
- 561 Korhonen O, Sawada D, Budtova T (2019) All-cellulose composites via short-fiber dispersion
562 approach using NaOH–water solvent. *Cellulose* 26:4881-93.
- 563 Kröling H, Duchemin B, Dormanns J, Schabel S, Staiger MP (2018) Mechanical anisotropy of
564 paper-based all-cellulose composites. *Compos Part A-Appl S* 113:150-7.
- 565 Labidi K, Korhonen O, Zrida M, Hamzaoui AH, Budtova, T (2019) All-cellulose composites from
566 alfa and wood fibers. *Ind Crop Prod* 127:135–141.
- 567 Langan P, Nishiyama Y, Chanzy H (2001) X-ray structure of mercerized cellulose II at 1 Å
568 resolution. *Biomacromolecules* 2:410–416.
- 569 Le KA, Rudaz C, Budtova T (2014) Phase diagram, solubility limit and hydrodynamic properties of
570 cellulose in binary solvents with ionic liquid. *Carbohydr Polym* 105:237-43.

571 Mat Salleh M, Magniez K, Pang S, Dormanns JW, Staiger MP (2017) Parametric optimization of
572 the processing of all-cellulose composite laminae. *Adv Manuf Polym Compos Sci* 3:73-9.

573 Nishino T, Matsuda I, Hirao K (2004) All-cellulose composite. *Macromolecules* 37:7683–7687.

574 Nishino T, Arimoto N (2007) All-cellulose composite prepared by selective dissolving of fiber
575 surface. *Biomacromolecules* 8:2712-6.

576 Nishiyama Y, Langan P, Chanzy H (2002) Crystal structure and hydrogen-bonding system in
577 cellulose I β from synchrotron X-ray and neutron fiber diffraction. *J Am Chem Soc*
578 124:9074–9082.

579 Newville M, Stensitzki T, Allen DB (2016) LMFIT: Non-linear Least-square Minimization and
580 Curve-fitting for Python; Astrophysics Source Code Library, Michigan Technological
581 University, Houghton, MI.

582 Piltonen P, Hildebrandt NC, Westerlind B, Valkama JP, Tervahartiala T, Illikainen M (2016) Green
583 and efficient method for preparing all-cellulose composites with NaOH/urea solvent.
584 *Compos Sci Technol* 135:153-8.

585 Ramakrishnan KR, Corn S, Le Moigne N, Jenny P, Slangen P (2020) Experimental assessment of
586 low velocity impact damage in flax fabrics reinforced biocomposites by coupled high-
587 speed imaging and DIC analysis. *Compos Part A-Appl S* 1:106137.

588 S. Vic-3D, ©Software (2007) Correlated solutions incorporated, Columbia.
589 <https://www.correlatedsolutions.com/vic-3d/>.

590 Sirviö JA, Visanko M, Hildebrandt NC (2017) Rapid preparation of all-cellulose composites by
591 solvent welding based on the use of aqueous solvent. *Eur Polym J* 97:292-8.

592 Soykeabkaew N, Arimoto N, Nishino T, Peijs T (2008) All-cellulose composites by surface selective
593 dissolution of aligned ligno-cellulosic fibres. *Compos Sci Technol* 68:2201-7.

594 Soykeabkaew N, Nishino T, Peijs T (2009) All-cellulose composites of regenerated cellulose fibres
595 by surface selective dissolution. *Compos Part A-Appl S* 40:321–328.

596 Spörl JM, Batti F, Vocht MP, Raab R, Müller A, Hermanutz F, Buchmeiser MR (2017) Ionic Liquid
597 Approach Toward Manufacture and Full Recycling of All-Cellulose Composites.
598 *Macromol Mater Eng* 303:1700335.

599 Sun CC (2008) Mechanism of Moisture Induced Variations in True Density and Compaction
600 Properties of Microcrystalline Cellulose. *Int J Pharm* 346:93– 101.

601 Sutton MA, Yan JH, Tiwari V, Schreier HW, Orteu JJ (2008) The effect of out-of-plane motion on
602 2D and 3D digital image correlation measurements. *Opt Laser Eng* 46(10):746-57.

603 Sutton MA, Orteu JJ, Schreier H (2009) Image correlation for shape, motion and deformation
604 measurements: basic concepts, theory and applications. Springer Science & Business
605 Media.

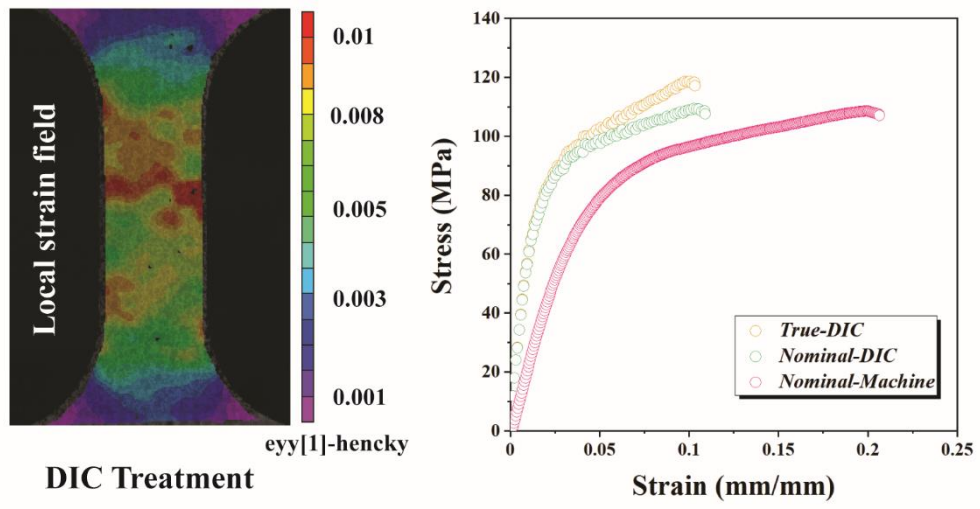
606 Xu D, Cerbu C, Wang H, Rosca IC (2019) Analysis of the hybrid composite materials reinforced
607 with natural fibers considering digital image correlation (DIC) measurements. *Mech Materi*
608 135:46-56.

609

610

611

TOC Image



612